This is a repository copy of *Non-fullerene acceptor fibrils enable efficient ternary organic solar cells with 16.6% efficiency*.

Version: Accepted Version

# Non-fullerene acceptor fibrils enable efficient ternary organic solar cells with 16.6% efficiency

Donghui Li[1,2], Xiaolong Chen[1,2], Jinglong Cai[1,2], Wei Li[1,2], Mengxue Chen[1,2], Yuchao Mao[1,2], Baocai Du[1,2], Joel A. Smith[3], Rachel C. Kilbride[3], Mary E. O'Kane[3], Xue Zhang[1,2], Yuan Zhuang[1,2], Pang Wang[1,2], Hui Wang[1,2], Dan Liu[1,2], Richard A. L. Jones[3], David G. Lidzey[3], Tao Wang[1,2]*

*1School of Materials Science and Engineering, Wuhan University of Technology, Wuhan 430070, China E-mail: twang@whut.edu.cn*

*2State Key Laboratory of Silicate Materials for Architectures, Wuhan University of Technology, Wuhan 430070, China*

*3Department of Physics and Astronomy, University of Sheffield, Sheffield, S3 7RH, UK*

ABSTRACT: Optimizing the components and morphology within the photoactive layer of organic solar cells (OSCs) can significantly enhance their power conversion efficiency (PCE). A new A-D-A type non-fullerene acceptor IDMIC-4F is designed and synthesized in this work, and is employed as the third component to prepare high performance ternary solar cells. IDMIC-4F can form fibrils after solution casting, and the presence of this fibrillar structure in the PBDB-T-2F:BTP-4F host confines the growth of donors and acceptors into fine domains, as well as acting as transport channels to enhance electron mobility. Single junction ternary devices incorporating 10 wt% IDMIC-4F exhibit enhanced light absorption and balanced carrier mobility, and achieve a maximum PCE of 16.6% compared to 15.7% for the binary device, which is a remarkable efficiency for OSCs reported in literature. This non-fullerene acceptor fibril network strategy is a promising method to improve the photovoltaic performance of ternary OSCs.

Keywords: ternary solar cells; non-fullerene acceptor fibrils; power conversion efficiency

# 1 Introduction

Organic solar cells (OSCs) have huge potential as renewable energy generators due to their flexible and light-weight nature, as well as the possibility for large-area fabrication by solution processing the photoactive layer [1–3]. The maximum achievable power conversion efficiency (PCE) of OSCs continues to improve as a result of extensive efforts on the synthesis of new semiconducting materials [4–6], morphological control [7], interfacial engineering [8–10] and innovations in device architecture [11,12], with PCEs over 16% being reported for single-junction binary OSCs [13–18]. Whilst the development of novel electron donors or non-fullerene acceptors is key to further enhance the efficiency of OSCs [19–21], component engineering and morphological optimization of the photoactive layer have also been demonstrated to be vitally important to achieve high performance [22–26].

The ternary blend strategy is a promising approach to engineer the components of the photoactive layer by incorporating a third component into a host donor:acceptor system [27–29]. Blending three light-absorbing materials which have complementary absorption spectra can enhance light harvesting to increase the short-circuit current density ($J_{SC}$) [30–32]. Some ternary systems show increased open-circuit voltage ($V_{OC}$) at the expense of $J_{SC}$, however PCE enhancements can be achieved by fine tuning the volume ratio of the third component [33–35]. Additionally, the third component can be used to modify the nanoscale morphology to reduce the density of traps and therefore decrease parasitic recombination, thereby enhancing the fill factor (FF) [36–39]. Ternary OSCs with one donor and two acceptors have been widely reported [40–43]. Studies in recent years have shown that the development of non-fullerene acceptors offer more choice of material candidates for use in ternary OSCs [5,44–46]. Compared with fullerene acceptors, non-fullerene acceptors possess higher tunability of energy levels and light absorption [47,48], providing more opportunities for the development of high-performance OSCs [49,50]. Recently, a non-fullerene acceptor BTP-4F (also known as Y6) was reported, and single-junction binary devices with an active layer comprising PBDB-T-2F (also called PM6) as the donor and BTP-4F as the acceptor have achieved 15.7% PCE [51]. This result has demonstrated the continuing potential for molecular engineering to enable high efficiency OSCs.

In this work, a new acceptor-donor-acceptor (A-D-A) type, non-fullerene acceptor IDMIC-4F is designed and synthesized. IDMIC-4F has a high tendency to form nanoscale fibrils after solution

casting, as well as exhibiting strong absorption from 600 to 800 nm which is complementary to that of PBDB-T-2F and BTP-4F. A series of inverted OSC devices are fabricated by incorporating a range of IDMIC-4F concentrations into the PBDB-T-2F:BTP-4F binary photovoltaic system to prepare ternary OSCs. The presence of this fibrillar IDMIC-4F in the ternary blend creates fine phase-separated domains with enhanced electron mobility. We find that although 10 wt% IDMIC-4F in ternary OSC blend (i.e., with a blend ratio of 1:1.08:0.12 in PBDB-T-2F:BTP-4F:IDMIC-4F) shows enhanced light absorption and balanced carrier mobility, the $V_{OC}$ gradually increases with the increasing IDMIC-4F content. A maximum PCE of 16.6% is achieved, with a $V_{OC}$ of 0.864 V, $J_{SC}$ of 25.8 mA/cm$^2$ and FF of 74.4%, which is a remarkable efficiency for single-junction OSCs. Our results suggest that the non-fullerene acceptor fibrillar channels formed in OSCs have great potential as a strategy to achieve efficiency gains in ternary blend solar cells.

## 2 Results and discussion

The chemical structures and energy levels of PBDB-T-2F, BTP-4F and IDMIC-4F are shown in **Figure 1a** and **b**. PBDB-T-2F has been proven to be an effective electron donor in high performance OSCs [52,53]. The electron acceptor BTP-4F employs a ladder-type, electron-deficient-core-based and central fused ring (dithienothiophen[3.2-b] -pyrrolobenzothiadiazole) with a benzothiadiazole (BT) core, and shows fine tunability in its absorption and electron affinity [51]. The IDMIC-4F molecule possesses seven fused rings and two difluoro-substituted end groups in the donating (D) and accepting (A) moieties, respectively. IDMIC-4F can be synthesized in five steps, with the synthesis routes shown in **Scheme S1**. The synthesis details and related characterization of IDMIC-4F are given in the supporting information. Nuclear magnetic resonance (NMR) spectra of various compounds are shown in **Figure S6-13**. The cyclic voltammogram of IDMIC-4F is shown in **Figure S1**, which determines the HOMO and LUMO energy levels at -5.46 and -3.83 eV, respectively. The absorption spectra of pure PBDB-T-2F, BTP-4F and IDMIC-4F films can be seen in **Figure 1c**. It is apparent that IDMIC-4F exhibits a strong photon-harvesting ability primarily between 600 to 800 nm, which is complementary to PBDB-T-2F and BTP-4F.

After solution casting from chloroform (CF), IDMIC-4F forms long aspect ratio fibrils, as determined using atomic force microscopy (AFM, **Figure 1d**) characterization method.

Grazing-incidence wide-angle X-ray scattering (GIWAXS) characterization (**Figure 1e** and **Figure S2**) of the pure IDMIC-4F film shows a number of diffraction rings in both out-of-plane and in-plane directions, suggesting that IDMIC-4F is highly crystalline. The diffraction rings located at $q_z$ of 0.43, 0.86 and 1.29 Å$^{-1}$ are indexed as the (001), (002) and (003) diffraction peaks of IDMIC-4F crystals. IDMIC-4F can retain its fibrillar structure after solution casting from its photovoltaic blend with PBDB-T-2F, as evidenced from the transition electron microscope (TEM) image in Fig. S3. The PBDB-T-2F:IDMIC-4F binary device gave a PCE$_{max}$ of 9.4%, with a J$_{SC}$ of 16.6±0.2 mA cm$^{-2}$, V$_{OC}$ of 0.890±0.01 V, and FF of 60.5±1.9%. This low efficiency is partly due to its low J$_{SC}$ value as IDMIC-4F barely absorbs light in the long wavelength range beyond 800 nm (see Fig. 1c), and the low FF is likely due to the rough interface with the anode (caused by the fibrillar structure of IDMIC-4F) that induces serious charge recombination. However, we believe that the fibril fragments of IDMIC-4F in the active layer of OSCs are likely to be desirable for bulk-heterojunction (BHJ) organic solar cells as they may act as pathways for efficient charge transport[54], which we continue to demonstrate through ternary OSCs by employing IDMIC-4F as the third component.
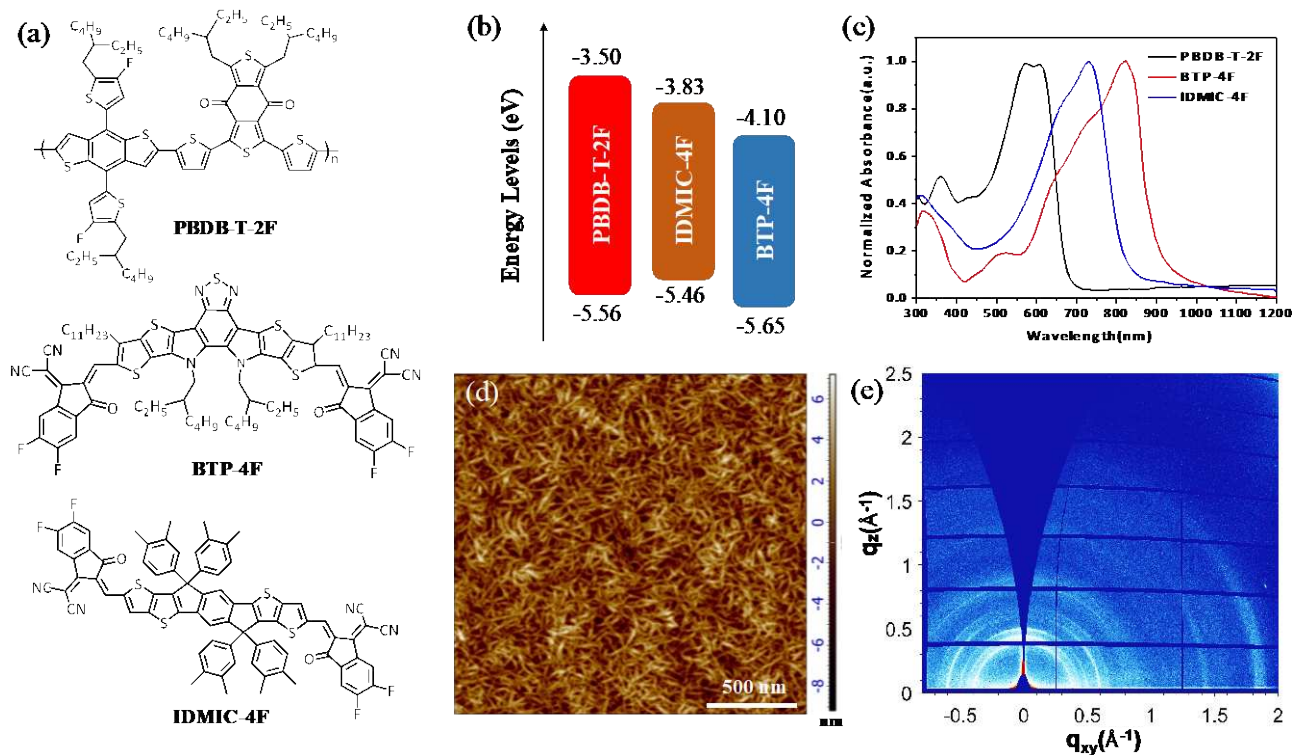


**Figure 1** (a) The chemical structures and (b) energy levels of PBDB-T-2F, BTP-4F and IDMIC-4F. (c) The absorption spectra of PBDB-T-2F, BTP-4F and IDMIC-4F pure films. (d) AFM, (e) 2D GIWAXS pattern for a pure IDMIC-4F film.

The photoactive layers of our ternary OSCs were prepared by fixing the weight ratio of electron donor (i.e. PBDB-T-2F) to electron acceptors (i.e., total content of BTP-4F and IDMIC-4F) at 1:1.2. The absorption coefficients of PBDB-T-2F:BTP-4F binary and ternary films with different contents of IDMIC-4F (weight ratio of IDMIC-4F over the total amount of BTP-4F and IDMIC-4F) are measured and shown in **Figure 2a**. The addition of IDMIC-4F results in increased absorption until the content of IDMIC-4F is over 10 wt%. This indicates that the introduction of an appropriate amount of IDMIC-4F increases light absorption of ternary OSCs due to its stronger absorption between 600 to 800 nm. The presence of more IDMIC-4F however reduces the light absorption of ternary blends as it is transparent in the long wavelength range over 800 nm. The photoluminescence (PL) spectra of BTP-4F, IDMIC-4F and BTP-4F:IDMIC-4F (10 wt%) blend films are shown in **Figure S5**. It can be seen that the maximum PL emission peaks of BTP-4F and IDMIC-4F locate at 840 and 920 nm respectively, and the PL peak of IDMIC-4F disappears from the spectrum of the BTP-4F:IDMIC-4F (10 wt%) blend film, suggesting energy transfer from IDMIC-4F to BTP-4F which will contribute to efficient photon utilization and the enhancement of device efficiency of ternary OSCs. IDMIC-4F therefore absorbs photons but then transfers the energy to BTP-4F, and exciton dissociation mainly occurs at the interface between PBDB-T-2F and BTP-4F, with holes and electrons are injected into anode and cathode via PBDB-T-2F and BTP-4F respectively. The current density-voltage (J-V) characteristics of ternary OSCs with different IDMIC-4F contents under AM 1.5G simulated solar light at 100 mW cm$^{-2}$ are plotted in **Figure 2b**, with the corresponding device metrics summarized in **Table 1**. For the binary system without any post-treatments, the PBDB-T-2F:BTP-4F devices have a maximum PCE (PCE$_{max}$) of 15.7% with an average J$_{SC}$ of 25.1±0.4 mA cm$^{-2}$, V$_{OC}$ of 0.855±0.01 V and FF of 73.0±0.3%. The ternary OSCs incorporating 5 wt% IDMIC-4F has an enhanced efficiency, with 10 wt% IDMIC-4F exhibiting a significantly improved PCE$_{max}$ of 16.6%, with an average J$_{SC}$ of 25.6±0.2 mA cm$^{-2}$, V$_{OC}$ of 0.864±0.01 V and FF of 74.2±0.1%. The V$_{OC}$ of ternary OSCs continuously increases with an increasing proportion of IDMIC-4F, and lies between the V$_{OC}$ values of PBDB-T-2F:BTP-4F and PBDB-T-2F:IDMIC-4F binary cells, in line with observations in many other ternary OSCs reported in the literature.[55–57] The FF and J$_{SC}$ values of the ternary OSCs, however, show strong dependence on the IDMIC-4F contents and reach their maxima with 10 wt% IDMIC-4F, indicating efficient charge transport channels in the blend as well as optimized photon harvesting at this composition.
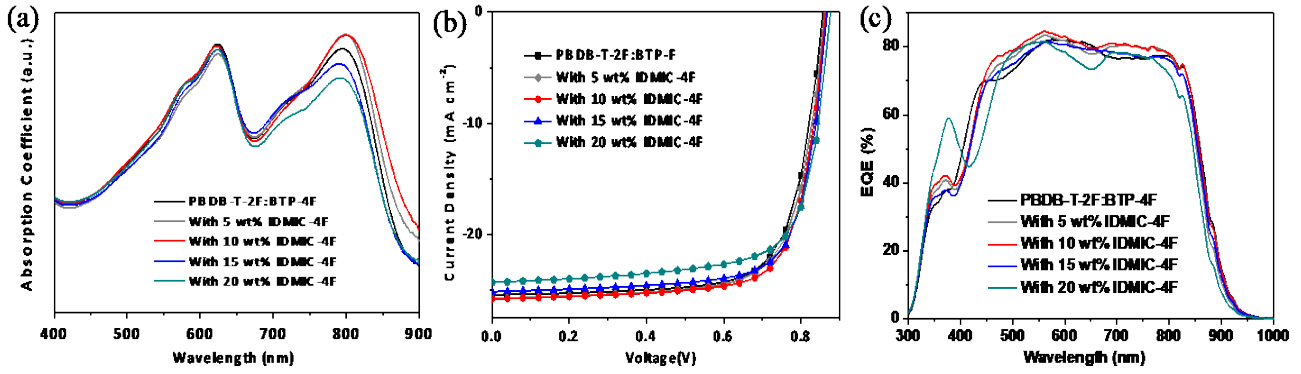
**Figure 2** (a) The absorption spectra of PBDB-T-2F:BTP-4F blends with different contents of IDMIC-4F. (b) J-V curves and (c) EQE of ternary OSCs with different contents of IDMIC-4F.

**Table 1** Photovoltaic parameters of ternary OSCs with different amount of IDMIC-4F. The average values and standard deviations were obtained from statistical analysis of over 20 individual devices.

| Component in active layer | Blending ratio | FF [%] | $J_{SC}$ [mA cm$^{-2}$] | Calculated $J_{SC}$ [mA cm$^{-2}$] | $V_{OC}$ [V] | PCE$_{avg}$ [%] | PCE$_{max}$ [%] |
|---|---|---|---|---|---|---|---|
| PBDB-T-2F:BTP-4F | 1:1.2 | 73.0±0.3 | 25.1±0.4 | 24.5 | 0.855±0.01 | 15.5±0.2 | 15.7 |
| PBDB-T-2F:BTP-4F with 5% IDMIC-4F | 1:1.14:0.06 | 73.1±0.3 | 25.4±0.3 | 24.6 | 0.858±0.01 | 15.9±0.2 | 16.1 |
| PBDB-T-2F:BTP-4F with 10% IDMIC-4F | 1:1.08:0.12 | 74.2±0.1 | 25.6±0.2 | 25.3 | 0.864±0.01 | 16.4±0.2 | 16.6 |
| PBDB-T-2F:BTP-4F with 15% IDMIC-4F | 1:1.02:0.18 | 73.9±0.4 | 24.8±0.2 | 24.6 | 0.867±0.01 | 15.8±0.4 | 16.2 |
| PBDB-T-2F:BTP-4F with 20% IDMIC-4F | 1:0.96:0.24 | 71.8±0.4 | 24.1±0.2 | 23.5 | 0.876±0.01 | 14.8±0.4 | 15.4 |
| PBDB-T-2F:IDMIC-4F | 1:1.2 | 60.5±1.9 | 16.6±0.2 | 16.1 | 0.890±0.01 | 8.9±0.3 | 9.4 |

The range and magnitude of the spectral response of the solar cells are characterized using external quantum efficiency (EQE) measurements, which are presented in **Figure 2c**. Those calculated $J_{SC}$ values from EQE spectra are summarized in **Table 1,** and are only *ca.* 5% less than

the $J_{SC}$ values obtained from J-V tests, hereby validating our J-V measurements. The EQE values of devices incorporating no more than 10 wt% IDMIC-4F are slightly increased over the wavelength range from 450 to 800 nm, with a broad response over the wavelength range from 300 to 950 nm. However, the EQE values start to decrease in the wavelength range over 430 nm when the fraction of IDMIC-4F exceeds 15 wt%, with an enhancement between 350 to 430 nm for the device with 20 wt% IDMIC-4F (which we believe as a result of morphology changes that are presented hereafter). Our results suggest that the content of IDMIC-4F must be carefully optimized in PBDB-T-2F:BTP-4F based ternary OSCs to achieve optimum device performance.

GIWAXS measurements are employed to investigate the molecular packing in the blend films and pure BTP-4F. The 2D GIWAXS patterns of blend films are presented in **Figure 3a-d**, with the corresponding 1D profiles in the out-of-plane (OOP) and in-plane (IP) directions presented in **Figure 3e, f**. From literature, pure PBDB-T-2F shows a (010) $\pi-\pi$ stacking peak at $q_z$=1.66 Å$^{-1}$, and a (100) scattering peak in IP direction at $q_{xy}$=0.30 Å$^{-1}$.[51,58] The pure BTP-4F film is characterized by a strong $\pi-\pi$ stacking peak at $q_z$=1.76 Å$^{-1}$, and two scattering peaks at $q_{xy}$=0.29 Å$^{-1}$ (associated with lamellar stacking) and $q_{xy}$=0.43 Å$^{-1}$ (associated with backbone ordering), which is a typical face-on orientation. The blend films exhibit a strong scattering peak at $q_z$=1.75 Å$^{-1}$ due to the $\pi-\pi$ stacking of BTP-4F,[16] together with a further scattering feature at $q_{xy}$=0.31 Å$^{-1}$ due to the lamellar stacking of either PBDB-T-2F or BTP-4F.[51] The diffraction peak at $q_{xy}$=0.43 Å$^{-1}$ of pure BTP-4F still persists in the PBDB-T-2F:BTP-4F binary blend film, but is absent in all ternary blend films. The intensities of (100) and (010) scattering peaks in the ternary films is maintained when the fraction of IDMIC-4F is 10 wt% or less, and then gradually reduces with further increases in IDMIC-4F content. Nevertheless, the face-on orientation has not been disrupted in the ternary blends, which is beneficial to guarantee efficient charge transport towards the electrodes [59,60]. We note that no scattering rings of IDMIC-4F are present in GIWAXS patterns for the ternary blend films, and we attribute this to the small-sized and well-dispersed IDMIC-4F fibrils (see TEM image in a later discussion) with a limited volume present in the ternary films and consequently low scattering intensity to be determined.
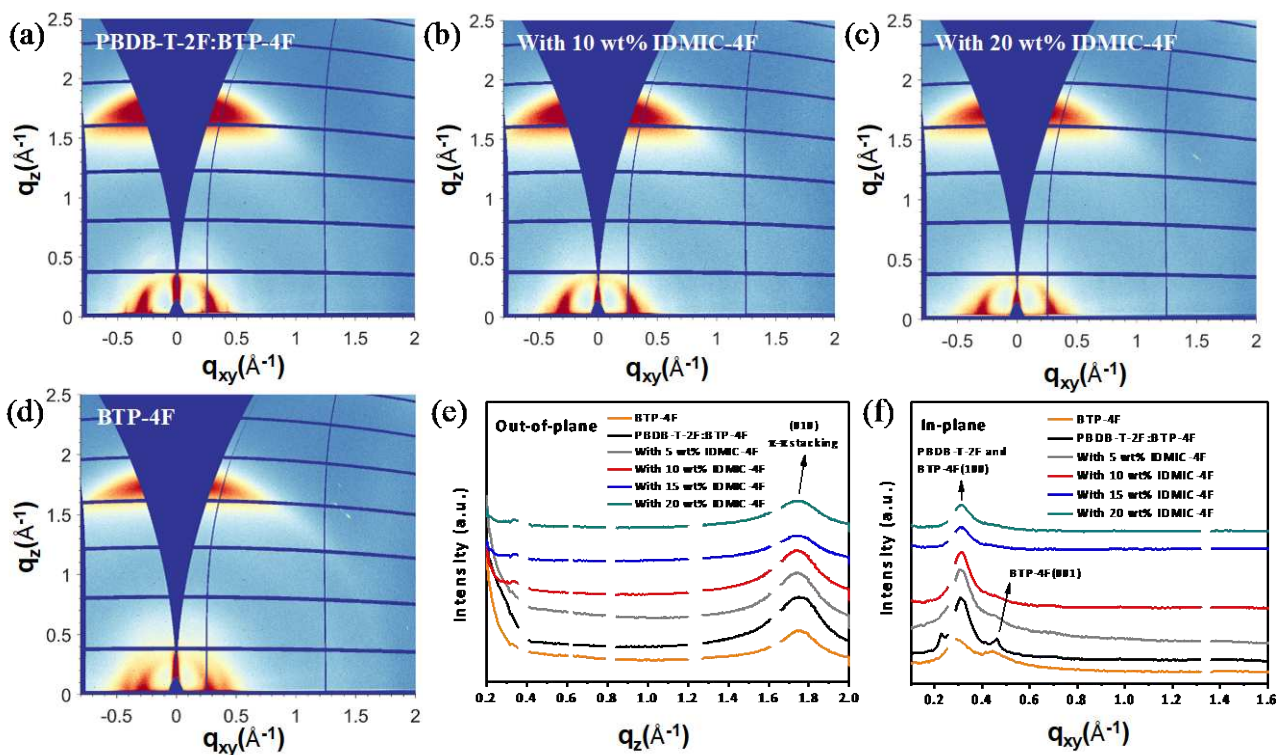
**Figure 3** GIWAXS 2D patterns of (a) PBDB-T-2F:BTP-4F film, and ternary blend films with (b) 10 wt%, (c) 20 wt% IDMIC-4F, (d) neat BTP-4F film and (e, f) intensity profiles along the out-of-plane and in-plane directions for the neat BTP-4F film and all blend films.

To visualize the IDMIC-4F fibrils in the ternary blends, TEM measurements were carried out on representative films to investigate their bulk morphology and are shown in **Figure 4a**, **b**. Due to the different electron densities, the electron donor and acceptor domains appear bright and dark respectively. The fibrillar structure of IDMIC-4F has been observed in its pure film, its binary blends with PBDB-T-2F and BTP-4F (see Figure S3 and S4), as well as the ternary blend films. The IDMIC-4F fibrils apparently affect phase separation within the blend films, and more importantly the fibril network acts as charge transport pathways to enhance device performance. To quantify the phase separated domain size within the ternary films, grazing-incidence small-angle X-ray scattering (GISAXS) measurements were conducted. Examples of the 2D GISAXS patterns are shown in **Figure 4c** and **d,** and 1D GISAXS profiles along the $q_{xy}$ axis (in-plane direction) for PBDB-T-2F:BTP-4F blends with different IDMIC-4F contents are shown in **Figure 4e**. We used the software SasView to fit the 1D GISAXS profiles in a universal model detailed in the supporting information, with fitting parameters summarized in **Table 2**. Here, the parameter ξ is the average correlation length of the PBDB-T-2F-rich phase, with η and D being the correlation length and

fractal dimension of acceptors respectively. $2R_g$ is the formulaic product of $\eta$ and $D$, and represents the size of the acceptor domain [61]. The modelled results show the correlation length ($\xi$) of PBDB-T-2F and the domain size of acceptors ($2R_g$) all decrease upon the addition of IDMIC-4F. We believe that the presence of IDMIC-4F fibrils confines the growth of donor and acceptor domains during the phase separation process after solution casting (see the scheme in **Figure 4f**), resulting in the increase of bulk heterojunction interfaces to allow exciton dissociation. The presence of fibrillar IDMIC-4F also helps to facilitate charge transport (*vide infra*). All such characteristics are beneficial in enhancing the efficiency of the photon to electron conversion process.
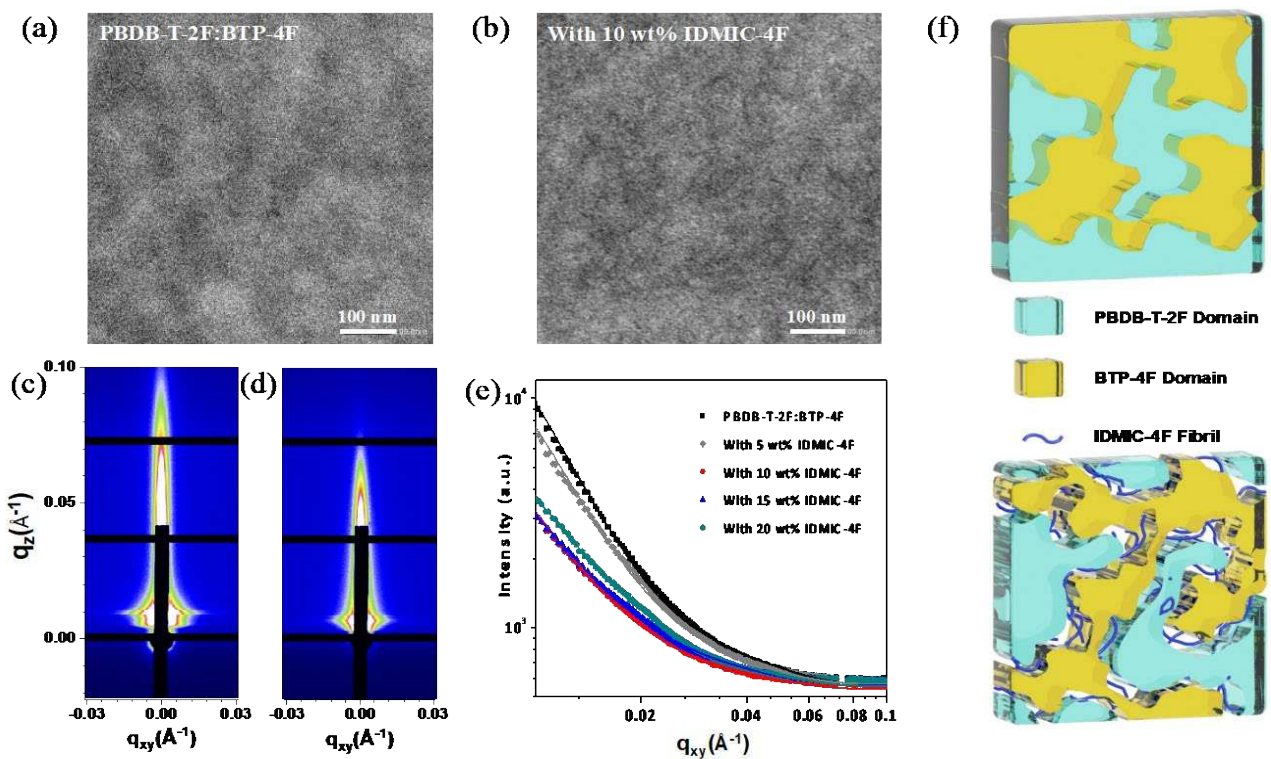


**Figure 4** TEM images of (a) PBDB-T-2F:BTP-4F blend, and its related ternary blend with (b) 10 wt% IDMIC-4F. 2D GISAXS patterns of (c) PBDB-T-2F:BTP-4F blend film, and (d) with the incorporation of 10 wt% IDMIC-4F. (e) 1D GISAXS profiles along $q_{xy}$ axis for PBDB-T-2F:BTP-4F blends with different IDMIC-4F contents. (f) Schematic illustration of the confinement effect of IDMIC-4F fibrils, which reduce phase separated domain sizes and act as charge transport channels.

**Table 2** Fitting parameters of 1D GISAXS profiles of the PBDB-T-2F:BTP-4F binary blend, and ternary blends with various amount of IDMIC-4F.

| Component | $\xi$ [nm] | $\eta$ [nm] | D | $2R_g$ [nm] |
|---|---|---|---|---|
| PBDB-T-2F:BTP-4F (1:1.2) | 15.3 | 15.1 | 2.7 | 74.0 |
| PBDB-T-2F:BTP-4F:IDMIC-4F (1:1.14:0.06) | 14.9 | 16.2 | 2.7 | 72.4 |
| PBDB-T-2F:BTP-4F:IDMIC-4F (1:1.08:0.12) | 14.6 | 16.0 | 2.6 | 69.2 |
| PBDB-T-2F:BTP-4F:IDMIC-4F (1:1.02:0.18) | 14.6 | 16.4 | 2.6 | 70.8 |
| PBDB-T-2F:BTP-4F:IDMIC-4F (1:0.96:0.24) | 14.6 | 16.3 | 2.6 | 70.5 |

In order to gain more insight of the exciton dissociation, charge transport and recombination in these devices, the dependence of J-V characteristics on light intensity were measured. **Figure 5a** shows the photocurrent density ($J_{ph}$) as a function of effective voltage ($V_{eff}$) of our devices. $J_{ph}$ is defined by $J_{Light} - J_{Dark}$, where $J_{Light}$ and $J_{Dark}$ represent the current densities under one sun illumination and dark condition respectively. $V_{eff}$ is defined by $V_0-V_a$, where $V_0$ is the voltage at $J_{ph} = 0$ and $V_a$ is the applied voltage. We can see from Figure 5a that the values of $J_{ph}$ saturates when $V_{eff}$ approaches 1 V, indicating that the electron-hole pairs are all effectively dissociated at this condition. P(E, T) can be calculated by $J_{ph}/J_{sat}$ to present the exciton dissociation efficiency. As shown in **Table 3**, the $J_{sat}$ with 10 wt% IDMIC-4F shows a larger value than others, and P(E, T) of the TSCs with 0, 5, 10, 15 and 20 wt% of IDMIC-4F are 97.7%, 98.0%, 98.1%, 98.1% and 97.8%, suggesting that a moderate incorporation of IDMIC-4F can enhance exciton dissociation. The $V_{OC}$ dependence of light intensity of TSCs is employed to evaluate charge recombination in these devices. The slopes of 1.52, 1.50 and 1.58 kT/q are obtained in the $V_{OC}$ versus light intensity plots of TSCs, as seen in **Figure 5b**, indicating that bimolecular recombination exist in all devices and the trap-assisted recombination is weaker in the TSC with 10 wt% IDMIC-4F.

The space charge-limited current (SCLC) method was also used to extract charge mobilities of binary and ternary active layers [62,63]. **Table 3** also shows the hole and electron mobilities ($\mu_h$ and $\mu_e$) obtained from dark J-V curves of electron-only and hole-only devices (**Figure 5c and d**). We find that $\mu_h$ of the blend film decreases monotonically, suggesting that the PBDB-T-2F molecular arrangement might be interrupted by incorporating IDMIC-4F. In contrast, the $\mu_e$ of the blend films increases monotonically from $3.1 \times 10^{-4}$ cm$^2$V$^{-1}$s$^{-1}$ to $8.2 \times 10^{-4}$ cm$^2$V$^{-1}$s$^{-1}$ with increasing amounts of IDMIC-4F. We attribute this enhanced $\mu_e$ to transport pathways provided by IDMIC-4F fibrils in the active layer. The $\mu_h/\mu_e$ ratio in the binary device is 2.45, and this value decreases to 0.92 for the ternary OSCs with 10 wt% IDMIC-4F, which indicates relatively balanced charge transport; a feature that is beneficial in reducing charge accumulation and recombination. This is expected to lead to an enhancement in FF; a finding confirmed by our experimental data.
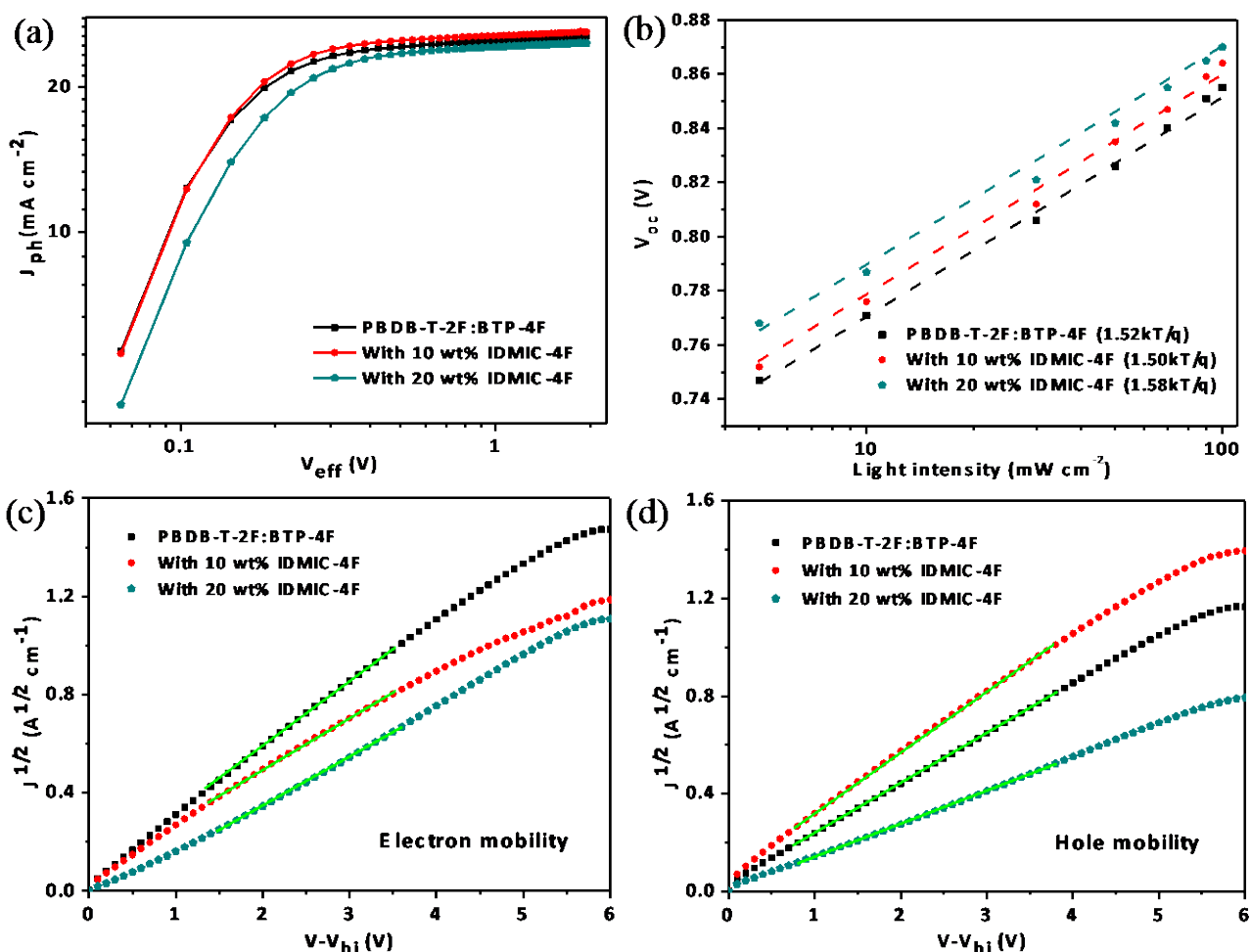


**Figure 5** (a) Photocurrent density versus effective voltage and (b) V$_{OC}$ versus light intensity for three blend compositions. Root square plots of (c) electron current densities versus bias voltage for ITO/ZnO/Active layer/Ca/Ag electron-only devices and (d) hole current densities versus bias voltage for ITO/PEDOT:PSS/Active layer/MoO$_3$/Ag hole-only devices.

**Table 3** $J_{sat}$, P(E, T), electron and hole mobilities of PBDB-T-2F:BTP-4F blend films with different contents of IDMIC-4F.

| Components | $J_{sat}$ [mA cm$^{-2}$] | P(E, T) [%] | Hole mobility ($\mu_h$) cm$^2$V$^{-1}$s$^{-1}$ | Electron mobility ($\mu_e$) cm$^2$V$^{-1}$s$^{-1}$ | $\mu_h/\mu_e$ |
|---|---|---|---|---|---|
| PBDB-T-2F:BTP-4F (1:1.2) | 26.0 | 97.7% | 7.6×10$^{-4}$ | 3.1×10$^{-4}$ | 2.45 |
| PBDB-T-2F:BTP-4F:IDMIC-4F (1:1.14:0.06) | 26.3 | 98.0% | 6.8×10$^{-4}$ | 3.7×10$^{-4}$ | 1.84 |
| PBDB-T-2F:BTP-4F:IDMIC-4F (1:1.08:0.12) | 26.3 | 98.1% | 6.9×10$^{-4}$ | 7.5×10$^{-4}$ | 0.92 |
| PBDB-T-2F:BTP-4F:IDMIC-4F (1:1.02:0.18) | 25.6 | 98.1% | 5.4×10$^{-4}$ | 7.9×10$^{-4}$ | 0.68 |
| PBDB-T-2F:BTP-4F:IDMIC-4F (1:0.96:0.24) | 24.8 | 97.8% | 2.1×10$^{-4}$ | 8.2×10$^{-4}$ | 0.26 |

## 3 Conclusions

In summary, a new non-fullerene acceptor IDMIC-4F has been designed and synthesized. IDMIC-4F exhibits primary absorption from 600 to 850 nm, and forms fibrils after solution casting in pure and blend films. IDMIC-4F is incorporated into a PBDB-T-2F:BTP-4F host blend and fibrils are also formed in the ternary photovoltaic system. The presence of these fibrils is found to cause a confinement effect to reduce the phase-separated domain sizes of both donors and acceptors. Moreover, such fibrils act as efficient charge transport pathways, leading to increased electron mobility and balanced charge transport. This allows us to demonstrate an impressive PCE of 16.6% with the incorporation of 10 wt% IDMIC-4F. Our work demonstrates that the use of non-fullerene acceptor fibrils is an effective strategy to produce high performance ternary solar cells.

## References

1.    Li G, Zhu R, Yang Y. *Nat Photonics*, 2012, 6: 153–161

2.    Cheng P, Wang R, Zhu J, Huang W, Chang S, Meng L, Sun P, Cheng HW, Qin M, Zhu C, Zhan X, Yang Y. *Adv Mater*, 2018, 30: 1705243

3.    Heeger AJ. *Adv Mater*, 2014, 26: 10–28

4.    Fu H, Wang Z, Sun Y. *Angew Chemie Int Ed*, 2019, 58: 4442–4453

5.    Hou J, Inganas O, Friend RH, Gao F. *Nat Mater*, 2018, 17: 119–128

6.    Lin Y, Wang J, Zhang ZG, Bai H, Li Y, Zhu D, Zhan X. *Adv Mater*, 2015, 27: 1170–1174

7.    Li W, Chen M, Cai J, Spooner ELK, Zhang H, Gurney RS, Liu D, Xiao Z, Lidzey DG, Ding L, Wang T. *Joule*, 2019, 3: 819–833

8.    Yan Y, Li W, Cai J, Chen M, Mao Y, Chen X, Gurney RS, Liu D, Huang F, Wang T. *Mater Chem Front*, 2018, 2: 1859–1865

9.    Bai Y, Zhao C, Chen X, Zhang S, Zhang S, Hayat T, Alsaedi A, Tan Z, Hou J, Li Y. *J Mater Chem A*, 2019, 7: 15887–15894

10.   Wang Y, Lan W, Li N, Lan Z, Li Z, Jia J, Zhu F. *Adv Energy Mater*, 2019, 9: 1900157

11.   Li M, Gao K, Wan X, Zhang Q, Kan B, Xia R, Liu F, Yang X, Feng H, Ni W, Wang Y, Peng J, Zhang H, Liang Z, Yip HL, Peng X, Cao Y, Chen Y. *Nat Photonics*, 2017, 11: 85–90

12.   Huang J, Wang H, Yan K, Zhang X, Chen H, Li CZ, Yu J. *Adv Mater*, 2017, 29: 1606729

13.   Cui Y, Yao H, Zhang J, Zhang T, Wang Y, Hong L, Xian K, Xu B, Zhang S, Peng J, Wei Z, Gao F, Hou J. *Nat Commun*, 2019, 10: 2515

14.   Fan B, Zhang D, Li M, Zhong W, Zeng Z, Ying L, Huang F, Cao Y. *Sci China Chem*, 2019, 62: 746–752

15.   Xu X, Feng K, Bi Z, Ma W, Zhang G, Peng Q. *Adv Mater*, 2019, 31: 1901872

16.   Yan T, Song W, Huang J, Peng R, Huang L, Ge Z. *Adv Mater*, 2019, 31: 1902210

17.   Lin Y, Adilbekova B, Firdaus Y, Yengel E, Faber H, Sajjad M, Zheng X, Yarali E, Seitkhan

A, Bakr OM, El‑Labban A, Schwingenschlögl U, Tung V, McCulloch I, Laquai F, Anthopoulos TD. *Adv Mater*, September 2019, 1902965

18. Li K, Wu Y, Tang Y, Pan M, Ma W, Fu H, Zhan C, Yao J. *Adv Energy Mater*, 2019, 9: 1901728

19. Li X, Pan F, Sun C, Zhang M, Wang Z, Du J, Wang J, Xiao M, Xue L, Zhang Z-G, Zhang C, Liu F, Li Y. *Nat Commun*, 2019, 10: 519

20. Li Z, Jiang K, Yang G, Lai JYL, Ma T, Zhao J, Ma W, Yan H. *Nat Commun*, 2016, 7: 1–9

21. Wu Y, Zheng Y, Yang H, Sun C, Dong Y, Cui C, Yan H, Li Y. *Sci China Chem*, (2019) doi:10.1007/s11426-019-9599-1

22. Xie Y, Huo L, Fan B, Fu H, Cai Y, Zhang L, Li Z, Wang Y, Ma W, Chen Y, Sun Y. *Adv Funct Mater*, 2018, 28: 1800627

23. Ye L, Xie Y, Weng K, Ryu HS, Li C, Cai Y, Fu H, Wei D, Woo HY, Tan S, Sun Y. *Nano Energy*, 2019, 58: 220–226

24. An Q, Ma X, Gao J, Zhang F. *Sci Bull*, 2019, 64: 504–506

25. Chang Y, Lau TK, Pan M-A, Lu X, Yan H, Zhan C. *Mater Horizons*, 2019, 6: 2094–2102

26. Zhou Z, Xu S, Song J, Jin Y, Yue Q, Qian Y, Liu F, Zhang F, Zhu X. *Nat Energy*, 2018, 3: 952–959

27. Li H, Lu K, Wei Z. *Adv Energy Mater*, 2017, 7: 1602540

28. Bi P, Hao X. *Sol RRL*, 2019, 3: 1800263

29. Dayneko S V., Hendsbee AD, Cann JR, Cabanetos C, Welch GC. *New J Chem*, 2019, 43: 10442–10448

30. Gasparini N, Lucera L, Salvador M, Prosa M, Spyropoulos GD, Kubis P, Egelhaaf H-J, Brabec CJ, Ameri T. *Energy Environ Sci*, 2017, 10: 885–892

31. Ma X, Mi Y, Zhang F, An Q, Zhang M, Hu Z, Liu X, Zhang J, Tang W. *Adv Energy Mater*, 2018, 8: 1702854

32. Su D, Pan M-A, Liu Z, Lau TK, Li X, Shen F, Huo S, Lu X, Xu A, Yan H, Zhan C. *Chem Mater*, 2019, 31: 8908–8917

33. Chen Y, Ye P, Jia X, Gu W, Xu X, Wu X, Wu J, Liu F, Zhu Z-G, Huang H. *J Mater Chem A*, 2017, 5: 19697–19702

34. Chen Y, Ye P, Zhu Z, Wang X, Yang L, Xu X, Wu X, Dong T, Zhang H, Hou J, Liu F, Huang H. *Adv Mater*, 2017, 29: 1603154

35. Gao J, Wang J, An Q, Ma X, Hu Z, Xu C, Zhang X, Zhang F. *Sci China Chem*, 2019, 2836

36. Gasparini N, Jiao X, Heumueller T, Baran D, Matt GJ, Fladischer S, Spiecker E, Ade H, Brabec CJ, Ameri T. *Nat Energy*, 2016, 1: 16118

37. Liu S, You P, Li J, Li J, Lee C, Ong BS, Surya C, Yan F. *Energy Environ Sci*, 2015, 8: 1463–1470

38. Zhang M, Gao W, Zhang F, Mi Y, Wang W, An Q, Wang J, Ma X, Miao J, Hu Z, Liu X, Zhang J, Yang C. *Energy Environ Sci*, 2018, 11: 841–849

39. Liu T, Luo Z, Chen Y, Yang T, Xiao Y, Zhang G, Ma R, Lu X, Zhan C, Zhang M, Yang C, Li Y, Yao J, Yan H. *Energy Environ Sci*, 2019, 12: 2529–2536

40. Zhang M, Ming R, Gao W, An Q, Ma X, Hu Z, Yang C, Zhang F. *Nano Energy*, 2019, 59: 58–65

41. Xiao Z, Jia X, Ding L. *Sci Bull*, 2017, 62: 1562–1564

42. Kan B, Yi YQQ, Wan X, Feng H, Ke X, Wang Y, Li C, Chen Y. *Adv Energy Mater*, 2018, 8: 1800424

43. Kumari T, Lee SM, Kang SH, Chen S, Yang C. *Energy Environ Sci*, 2017, 10: 258–265

44. Sun J, Ma X, Zhang Z, Yu J, Zhou J, Yin X, Yang L, Geng R, Zhu R, Zhang F, Tang W. *Adv Mater*, 2018, 30: 1707150

45. Cheng P, Li G, Zhan X, Yang Y. *Nat Photonics*, 2018, 12: 131–142

46. Chang Y, Lau TK, Pan MA, Lu X, Yan H, Zhan C. *Mater Horizons*, 2019, 6: 2094–2102

47. Cheng P, Yan C, Wu Y, Wang J, Qin M, An Q, Cao J, Huo L, Zhang F, Ding L, Sun Y, Ma W, Zhan X. *Adv Mater*, 2016, 28: 8021–8028

48. Xie Y, Yang F, Li Y, Uddin MA, Bi P, Fan B, Cai Y, Hao X, Woo HY, Li W, Liu F, Sun Y. *Adv Mater*, 2018, 30: 1803045

49. Yu R, Yao H, Hou J. *Adv Energy Mater*, 2018, 8: 1702814

50. Huang H, Yang L, Sharma B. *J Mater Chem A*, 2017, 5: 11501–11517

51. Yuan J, Zhang Y, Zhou L, Zhang G, Yip HL, Lau TK, Lu X, Zhu C, Peng H, Johnson PA, Leclerc M, Cao Y, Ulanski J, Li Y, Zou Y. *Joule*, 2019, 3: 1140–1151

52. Zhang Y, Yao H, Zhang S, Qin Y, Zhang J, Yang L, Li W, Wei Z, Gao F, Hou J. *Sci China Chem*, 2018, 61: 1328–1337

53. Zhang S, Qin Y, Zhu J, Hou J. *Adv Mater*, 2018, 30: 1800868

54. Xia T, Cai Y, Fu H, Sun Y. *Sci China Chem*, 2019, 62: 662–668

55. Street RA, Davies D, Khlyabich PP, Burkhart B, Thompson BC. *J Am Chem Soc*, 2013, 135: 986–989

56. Khlyabich PP, Burkhart B, Thompson BC. *J Am Chem Soc*, 2011, 133: 14534–14537

57. Khlyabich PP, Rudenko AE, Thompson BC, Loo YL. *Adv Funct Mater*, 2015, 25: 5557–5563

58. Li Y, Wang Y, Zhang M, Guo X, Russell TP, Fan Q, Jiang Y, Su W, Guo B, Liu F. *Sci China Chem*, 2018, 61: 531–537

59. Ye L, Xiong Y, Zhang Q, Li S, Wang C, Jiang Z, Hou J, You W, Ade H. *Adv Mater*, 2018, 30: 1705485

60. Ma W, Yang C, Gong X, Lee K, Heeger AJ. *Adv Funct Mater*, 2005, 15: 1617–1622

61. Xiao Y, Lu X. *Mater Today Nano*, 2019, 5: 100030

62. Liu T, Huo L, Sun X, Fan B, Cai Y, Kim T, Kim JY, Choi H, Sun Y. *Adv Energy Mater*, 2016, 6: 1502109

63. Lu L, Luo Z, Xu T, Yu L. *Nano Lett*, 2013, 13: 59–64